Microstresses and microstructure in thick cobalt-based laser deposited coatings

de Oliveira, U.; Ocelik, Vaclav; De Hosson, J.T.M.

IMPORTANT NOTE: You are advised to consult the publisher's version (publisher's PDF) if you wish to cite from it. Please check the document version below.

Document Version
Publisher's PDF, also known as Version of record

Link to publication in University of Groningen/UMCG research database

Microstresses and microstructure in thick cobalt-based laser deposited coatings

U. de Oliveira, V. Ocelík *, J.Th.M. De Hosson

Department of Applied Physics, Netherlands Institute for Metals Research, University of Groningen, Nijenborgh 4, 9747 AG Groningen, The Netherlands

Abstract

Microstresses in a thick laser clad Co-based coating on steel substrate were investigated with 3D X-ray microscopy using an intense synchrotron microfocused beam. The microstructure was examined with light microscopy and field emission scanning electron microscopy equipped with X-ray energy dispersive spectroscopy and Electron Back Scattering Diffraction (orientation imaging microscopy). Microhardness and scratch resistance variations inside the coating are related to the local microstructure influenced by additional heating and by melt convection during the laser track overlapping. The residual microstrains were accessed with a high spatial resolution defined by the size of the synchrotron microbeam. Type II residual strains and stresses on the level of individual grains and dendrites were analyzed in terms of tensor invariants, hydrostatic and von Mises shear stress, along the depth of a slightly diluted clad track. The upper part of the coating shows a constant spread of hydrostatic stresses between −500 and 500 MPa; towards the bottom of the track the spread of these stresses increases almost linearly with depth. A correlation between the microstructural features and the spread of the hydrostatic microstresses was found. It is concluded that microstresses in individual neighboring grains are inhomogeneously dispersed.

1. Introduction

The laser cladding technique consists of producing a protective layer on the surface of the metallic substrate using a high power laser as heat source while a powder stream is blown under the laser beam [1,2]. The substrate is scanned by the laser that creates a melt pool with a height corresponding to the thickness of a single clad track. To attain full coverage of the substrate, single tracks are consecutively overlapped. Residual stresses are generated mainly during the solidification stage of the melt. In the case that the shrinkage of the melt pool is higher than the expansion effects caused by other phase transformations, tensile residual stresses predominate [3] and the coating may crack if these overcome the fracture stress. In order to avoid cracking and to further improve the properties of laser clad coatings a precise evaluation of residual stresses and its evolution is an important objective of research.

It is well known that the residual stress tensor can be examined with radiation diffraction techniques. The stresses are classified in three types [4,5] according to the length scale in the material. The choice of the most suitable analysis technique depends on the type of stress that one wants to investigate [6]. Residual stresses of first order, type I stress or macrostresses, are homogeneous over a large number of grains and a balance of forces is assumed over a large number of crystals. For the investigation of these stresses the diffraction of lab X-rays or neutron can be applied. Laboratory X-rays [4,7,8] is a relatively cheap alternative for the investigation of macrostresses but it limits the analysis to the surface, i.e. to a biaxial stresses tensor analysis. Neutron beams [9] have a high penetration depth and allow the investigation of bulk properties. Residual stresses of second order, type II stress, are considered homogenous inside one grain and the forces involved are in balance among neighboring grains. Finally, residual stresses of third order, type

* Corresponding author.
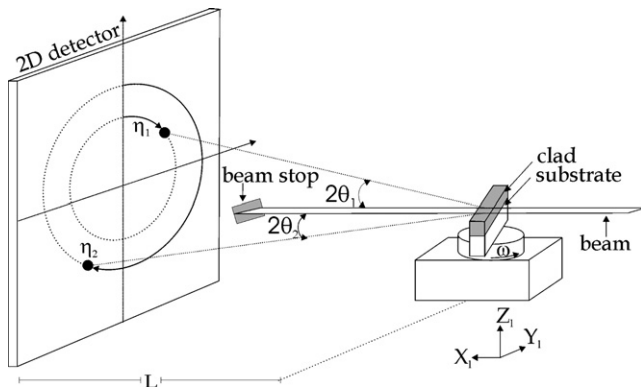*E-mail address:* v.ocelik@rug.nl (V. Ocelík).

Fig. 1. Schematics of 3DXRD microscope experimental setup.

III stress, are homogeneous over some interatomic distances and the internal forces are in balance around crystalline defects. Type II as well as III stresses are termed microstresses. For fine-grained, polycrystalline materials, the most suitable technique to detect bulk, intergranular microstrains is diffraction of synchrotron hard X-rays that can operate with high spatial resolution [6,10] and are intense enough to achieve bulk penetration.

In this work, the applicability of the so-called Three-Dimensional X-ray Diffraction microscopy (3DRXD micros-copy) [11–15] was tested to measure microstresses in the bulk of a laser deposited γ-Co based clad track on a C45 steel substrate. A comparison between microstructural features observed by 3DXRD microscopy and by Orientation Imaging Microscopy (OIM) is performed for complementation of the analysis.

2. Experimental methods and data treatment

2.1. Laser cladding, microstructure characterization and properties measurements

A hardfacing Co–W–Cr alloy powder, Eutrolloy 16012, was deposited on C45 middle-carbon steel substrates by a computer controlled laser cladding system consisting of a powder feeder Sulzer Metco Twin 10 C, side cladding nozzle, XYZ-Rotation CNC table and the 2 kW continuous wave Nd:YAG Rofin Sinar laser. The processing parameters for the deposition of the sample were: laser power 1500 W, 4.2 mm diameter spot of defocused laser beam, scanning speed 5.0 mm/s and powder feeding rate 150 mg/s. More details concerning the laser processing and chemical composition of substrate, powder and produced coating may be found elsewhere [16].

The cladding sample for residual strain analysis was formed by two overlapped laser tracks. The first deposited track was diluted with iron from the substrate, while in the second track the degree of dilution was enough for metallurgical bonding, around 3–5%. It conserved the composition of the original hard facing alloy powder. For this reason, this track was used for the analysis of the residual stresses. The sample was prepared by spark-cutting erosion of 1 mm thick slice perpendicular to the cladding direction that was gently polished and cleaned in an ultrasonic bath to remove oxides created during the cutting

process. Furthermore, clad layers composed of 9 tracks with 2.0 mm overlap displacement were deposited on a 60 mm round bars for mechanical testing. Microhardness and scratch tests were carried out using a CSM Revetest scratch tester. Microhardness was measured using a Vicker's diamond indenter using a maximal load of 2 N and loading time of 15 s. A Rockwell indenter with a radius of 200 μm, 20 N constant normal load and scratching speed of 0.16 mm/s was used in several scratch tests. Microstructure of the laser coating was studied by optical microscopy, field emission scanning electron microscopy (Philips XL30) with Oriented Image Microscopy attachment (TSL) and X-ray energy dispersed spectroscopy (EDS). Samples for microstructural observations were cut transversally or longitudinally to the laser cladding direction, mechanically ground, subsequently polished by diamond suspensions (9, 6 and 3 μm sized) and finally polished using an OPS silica suspension. Long time final polishing with OPS was the best method to prepare the sample surface for electron back scatter diffraction observations.

2.2. 3DXRD microscopy set-up

Three-dimensional X-ray Diffraction (3DXRD) microscopy is a novel technique that combines high penetration, high intensity and high spatial resolution provided by hard X-rays from third generation synchrotron sources. The basic concepts of this technique are detailed in [11,12].

Fig. 1 illustrates the setup of our 3DXRD experiment using the beam line ID-11 at the ESRF Grenoble. A monochromatic beam of 80.4 kV, λ=0.15422 Å, was applied with a focus area of 30×20 μm. The sample is placed on an XYZ moving table mounted on an ω rotation stage. If ω is equal to 0° the direction of the beam coincides with the laser cladding direction. The X-ray beam is applied perpendicular to the ω rotation axis and the alignment of the table was performed with a thin capillary filled with the clad alloy powder. The diffraction patterns from irradiated grains are observed on a two-dimensional CCD detector of 100×100 mm surface area with a pixel size of 48.8 μm. To obtain diffraction from grains that are inside the irradiated volume the sample was analyzed in steps of Δω of 1° between −30 to 30° and 150 to 210°. The diffraction patterns from the coating were registered during 3 seconds in each rotation step. For the complete mapping the sample was translated along the Y and Z axis and the rotation routines was repeated.

The basic equation describing the diffraction in laboratorial system is [11]:

$$G_l^j = \Omega S U^j B G_{hkl}, \tag{1}$$

where:

- $\mathbf{G}_l^j$ is the measured scattered vector of the grain j in the laboratory reference system.
- $\mathbf{G}_{hkl}$ is the scattered vector in reciprocal space.
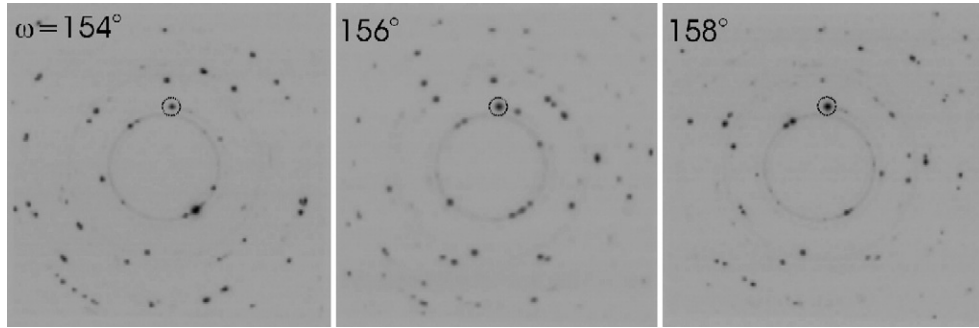- Ω is the coordinate transformation matrix between laboratory and the turntable ω axis.

Fig. 2. Diffraction patterns of γ-Co based alloy clad layer registered by 2D CCD detector during sample rotation of 1° range. The corresponding ω values are given in the inserts. The gradual increase of spot intensity is indicated in the circled (200) spot along the sequence.

- S is the sample system matrix fixed with respect to the sample preparation axis (RD, TD, ND).
- U^j is the unknown crystallographic orientation matrix of a diffracting grain j with respect to the sample in Euler angles representation.
- B is the matrix, which transforms the crystallographic system from reciprocal to real space.

For each set of rotations GRAINDEX, a computer program described in [11], is able to select the diffraction points of the grains that remain inside the irradiated area defined by the size of the incoming beam. These grains are indexed with the respective reflections and characterized by the orientation matrix U^j.

Fig. 2 shows the patterns acquired from three near ω values. Diffraction takes place when the Bragg's law is fulfilled, i.e. the reciprocal lattice points lay or are close the Ewald sphere. The continuous intersection of the scattered vectors with the Ewald sphere during the controlled rotation of the sample is observed

Fig. 3. Cumulative diffraction pattern from Co-based laser clad coating and the correspondent indexed γ-Co grains.

in the experiment as a gradual variation of spots' brightness as Fig. 2 indicates.

The data handling starts with a tracking and indexing algorithms, see [11]. First, images were corrected for distortion, illumination and an intensity threshold was defined. The tracking algorithm identified the diffraction spots on the images when their intensity was above the predefined threshold. The centers of gravity of these spots were defined as their positions in the laboratorial system. Only those points that match crystallographic reference data are considered for further analysis. Spots collected at different ω's that superpose each other are considered to originate from the same grain. Their centers of mass in laboratory coordinates are assigned from the strongest spot and the corresponding ω was recorded. The scattered vectors in lab coordinates, G_l^j, can then be calculated from the coordinates of these spots and the values of θ and η are inferred.

The indexing algorithm [12] is able to find grains, which fulfill the diffraction conditions by scanning through all possible rotations of single grain and their match with observed cumulative diffraction pattern represented by Eq. (1). When calculated and observed diffraction spots match inside the predefined criteria the grain j is identified and associated with its orientation matrix U^j. The stress-free lattice parameter 3.58122 Å of the γ-Co based alloy powder was used as input for indexing and posterior residual strains calculations. The minimum number of reflections for the identification of one grain was defined as 10. Fig. 3 is an example of the grains indexed with the data collected in one rotation routine. All positions of the identified diffraction peaks are plotted, but only those grains that scored 10 spots or more are indexed with an orientation matrix U^j.

2.3. Determination of microstrains and calculation of microstresses

The residual strains for each lattice family of planes are calculated from the measured shift of diffraction peaks by the differentiate form of the Bragg law [15].

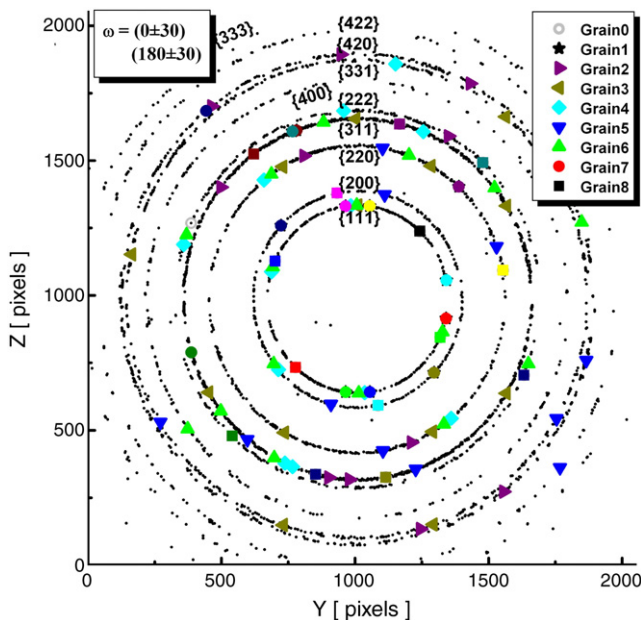$$\varepsilon_i = \frac{d_i - d_0}{d_0} = -\cot\theta_i \cdot \Delta\theta_i, \tag{2}$$

Table 1
Stiffness constants of γ-Co single crystal in GPa [19]

Constant	Theoretical	Experimental
C_{11}	234.2	242.0
C_{12}	176.2	160.0
C_{44}	111.4	128.0

where d_0 is the distance between diffracting planes of a reference stress-free material. The terms d_i and θ_i are the lattice spacing and diffraction angle of a family of planes from stressed grains. $\Delta\theta_i$ equals to $\theta_i - \theta_0$ and it is the angular shift of the diffraction peaks from the stressed to the stress-free grain.

These strains ε_i are given in each grain by the direction cosines l_i, m_i, and n_i, of the normal to the corresponding plane and the strain tensor of the grain [15]:

$$\varepsilon_i = \begin{pmatrix} l_i & m_i & n_i \end{pmatrix} \begin{pmatrix} \varepsilon_{11} & \varepsilon_{12} & \varepsilon_{13} \\ \varepsilon_{12} & \varepsilon_{22} & \varepsilon_{23} \\ \varepsilon_{13} & \varepsilon_{23} & \varepsilon_{33} \end{pmatrix} \begin{pmatrix} l_i \\ m_i \\ n_i \end{pmatrix} \quad (3)$$

Eqs. (2) and (3) define the basic system of linear equations for six unknowns: ε_{11}, ε_{22}, ε_{33}, ε_{12}, ε_{13}, ε_{23}. As the minimum number of (hkl)s defined to index the grain was 10, this system of equations is (over)determined and therefore solvable.

Moreover Eq. (3) can be expanded [15] in order to include the influence of the position of the centre of diffracted grains (ΔX, ΔY) on the shifts of diffraction peaks:

$$-\cot\theta_i \cdot \Delta\theta_i = \begin{pmatrix} l_i & m_i & n_i \end{pmatrix} \begin{pmatrix} \varepsilon_{11}^* & \varepsilon_{12}^* & \varepsilon_{13}^* \\ \varepsilon_{12}^* & \varepsilon_{22}^* & \varepsilon_{23}^* \\ \varepsilon_{13}^* & \varepsilon_{23}^* & \varepsilon_{33}^* \end{pmatrix} \begin{pmatrix} l_i \\ m_i \\ n_i \end{pmatrix} \quad (4)$$

$$-\{[\cos(\omega_i) + \sin(\omega_i)\sin(\eta_i)/\tan(\theta_i)] \cdot (\Delta X/L)$$

$$+[\sin(\omega_i) + \cos(\omega_i)\sin(\eta_i)/\tan(\theta_i)] \cdot (\Delta Y/L)\}$$

The components of strain tensor inside each indexed grain and relative position of this grain towards rotation axis were found by the singular value decomposition [17] applied to this (still overdetermined) system of linear Eq. (4). In a single grain the linear elastic relation between the stress and the strain tensor is given by Hooke's law [18] with the corresponding elastic constants. In general it has 21 independent components [18,19]. The number of components, however, can be further reduced according to the symmetry of the system. For a cubic crystal three independent components C_{11}, C_{12} and C_{44} are sufficient to describe the system. The theoretical and experimental values of stiffness coefficients C_{11}, C_{12} and C_{44} found in [20] are shown in Table 1. In our calculations experimental values were used.

3. Results and discussion

3.1. Microstructural characterization

Fig. 4a and b show the microstructure of the examined Co-based coating on the transversal cross-section. Fig. 4a is an optical micrograph from the interface between steel substrate and coatings. It shows that the interface is straight, sharp and without any macroscopic defects. Details of the microstructure of the central part of the coating are shown in the SEM micrograph depicted in Fig. 4b. γ-Co rich dendrites with typical size of 5 μm are positioned in fine interdentritic eutectic composed of γ-Co and carbidic phases. Because Fig. 4b is the SEM image taken in mixed (80% back scattered electrons – BSE mode and 20 % secondary electrons – SE mode) detector mode, the white spots in Fig. 4b indicate the higher amount of the heavy element W. Detailed description of the microstructural features observed in similar coatings by SEM, TEM, diffraction of lab and synchrotron X-rays were published elsewhere [16,21]. In connection with these results, the white spots in Fig. 4b represent the Co_6W_6C phase.

Orientation Imaging Microscopy (OIM) revealed the geometrical features and further details of the microstructure. Fig. 5 is the Inverse Pole Figure (IPF) that represents the relation of grain system with respect to the sample system. A cross section of two subsequent laser tracks perpendicular to laser cladding direction is shown. The first track (left) is overlapped by a second one with the same laser cladding parameters. Due to overlapping, the second track undergoes an elevation effect on the substrate and becomes less diluted. The [001] inverse pole figure was chosen to show the alignment of the grains with the laser cladding direction. The relation is given
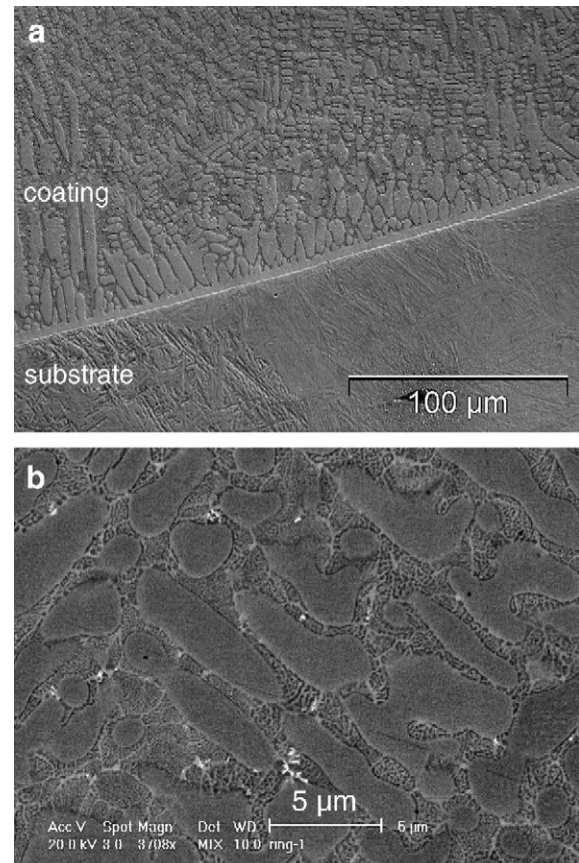

Fig. 4. a) OM micrograph from the coating/substrate interface. b) SEM micrograph from the central area of laser track.
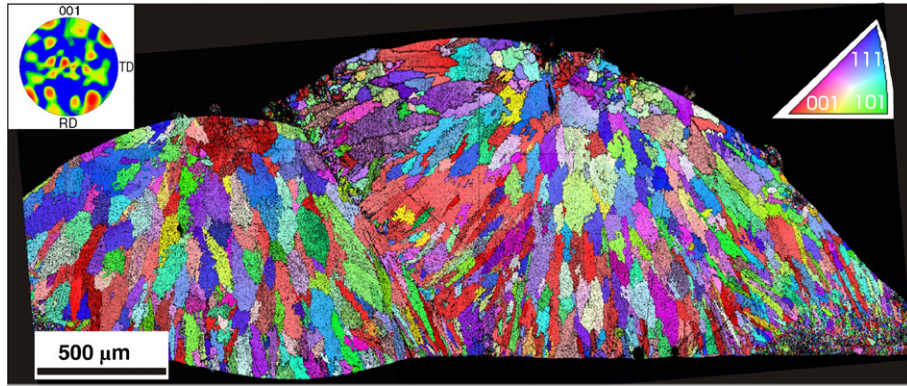
Fig. 5. Oriented Image Microscopy characterization of transversal cross section of double track laser clad sample represented by [001] Inverse pole figure.

on the color coded map on the upper right side of the figure. No preferential texture was detected as indicated also by the pole figure (PF) on the left upper corner of the figure. The fine dendritic microstructure shown in Fig. 4 belongs to relatively coarse grains that can be divided into two regions. In the upper part of the laser tracks, equiaxial grains with diameter of the order of 150 µm predominate. Towards the interface with the substrate the grains become finer and elongated. The size and geometrical features of the grains reflect the local solidification conditions. Cubic dendritic grains grow preferentially along a specific crystallographic direction that is the most aligned to the heat flow direction [22]. The coarser and equiaxial grains from the upper part are formed at the final stage in the cladding and undergo slower and isotropic heat extraction, while in the bottom part grains are formed fast and in the direction oriented of the solidification front. When the second track is deposited the laser remelts part of the first track belonging to the overlap area and the substrate so that a metallurgical bond is created. The redistribution of energy provokes a lifting effect of the second track that becomes less diluted than the previous one. This processing setup generated a second track with 3 to 5% dilution, enough for a metallurgical bonding with the substrate and conservation of the composition of the original alloy. The microstructure in the overlapping area of two tracks is similar to the microstructure close to the clad/substrate interface. The interface between two subsequent laser tracks is straight, well defined, poreless and no substantial variation of chemical composition could be detected by EDS.

Mechanical tests to link the microstructure with the mechanical properties were performed on the cross-section of clad layer composed of 9 tracks. The hardness distribution inside the clad was characterized by horizontal micro-indentation profiles performed at different depths of the coating.
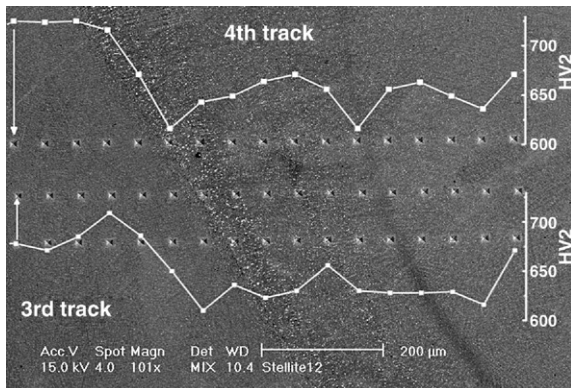

Fig. 6. SEM micrograph from the overlapping area between 3rd and 4th laser track with 3 rows of Vickers microhardness indents in horizontal direction. Hardness value profiles for upper and central row are also indicated.
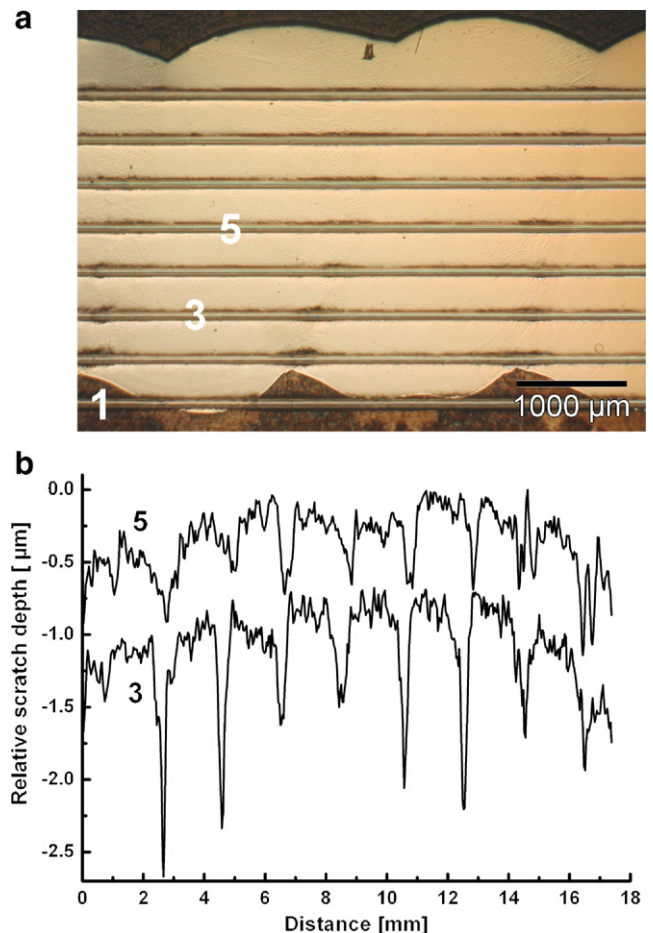
Fig. 7. a) Optical microscopy of 8 horizontal scratches made by CSM Revetester on a slanted cross section of laser clad coating with overlapping laser tracks. b) Comparison of relative scratch depths on scratch No. 3 and 5.
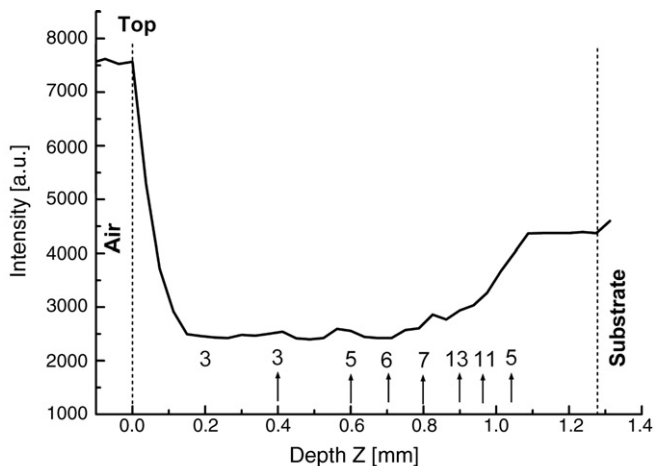
Fig. 8. Beam attenuation depth profile of the 2nd track of cladding sample. The arrows point to the exact location where 3DXRD microscopy measurements were performed and a number of successfully indexed grains is given at corresponding depth.

The averaged hardness measured in the center of the coating achieved value of 700 HV2 but presented considerable fluctuations on the overlap between two tracks. Fig. 6 illustrates details of microstructure and hardness profile measurement in the overlap area. Dispersion of white spots very close to the tracks interface is visible in Fig. 6, which means that W-rich carbides are preferentially formed in this area but the overall chemical composition characterized by EDS is the same as in the rest of the coating. This fact leads to the conclusion that due to a different thermal history in this area tungsten forms larger W rich carbides with the surrounded areas depleted of W. Microstructural softening was detected here as the hardness profiles in Fig. 6 indicate. Because the hardness values in Fig. 6 represent the local hardness, i.e. at a specific location in the coating, it is not possible to estimate the hardness via multiple Vicker's indents and by making a statistical evaluation of the error. However, an error of multiple measurement of the size of the same indent is very small ∼2%. The second drop in the hardness was detected on the dark curved band, which was proved by EDS as an area with local increase of iron content originated from the substrate.

The softening effect in laser tracks overlapping areas becomes more evident in scratch tests. The samples for this measurement were cut under a slanted angle to the cladding direction to achieve a larger area for tests. Eight scratch tests were performed from the bottom (1) to the (8) top of the coating,

Fig. 7a and b. It is apparent that the width of the scratches increases in the overlap area and this effect is more evident when the scratch is closer to the substrate. Fig. 7b shows the scratch depth along the scratches No. 3 and 5. A periodic increase of scratch depth is evident for both scratches with regular distance of 2 mm, which corresponds to the displacement between adjacent laser tracks. This feature, however, is less pronounced in scratch No. 5, which is further from the substrate than No. 3. The softening effects registered by the mechanical tests point to the presence of: a heat affected zone identified by the presence of coarse white W-rich dispersed eutectics; and an Fe-rich band in the overlap area between tracks caused by non-homogeneous mixing of the molten clad and substrate material that can take place in fast resolidification processes [23].

3.2. 3DXRD microscopy results

3DXRD measurements were performed on a double track cross-section starting from the top of the second laser track and gradually approaching the substrate in a direction perpendicular to the cladding direction (vertical direction on Fig. 5). Fig. 8 shows the attenuation profile of the transmitted synchrotron beam during movement along the Z-axis of the sample, being $Z=0$ on the top of the second laser track. A significant decrease of the attenuation is registered above 1 mm depth caused by dilution with Fe from the substrate.

The microstrain tensors and relative positions of the grain centers were calculated for all indexed grains solving the set of Eq. (4). Above 1.0 mm no grains could be indexed inside the tolerances given *a priori* to the algorithm routine. The orientations and relative positions of the center of all successfully indexed grains are plotted for three different depths on Fig. 9. The values ΔX, ΔY for relative position of centers of diffracted grains reflect the horizontal size of diffracted volume given by the width of focused beam of approximately 30 μm. However, the overall lateral resolution is determined by the size of the focused beam and by the rotation of the sample during diffraction experiment.

It is clear from Figs. 8 and 9 that the number of indexed grains increases with the depth. This is in agreement with OIM observations shown in Fig. 5, where grain size decreases with depth of the laser clad. Therefore the number of grains, which stay inside a diffracted volume during a ω-rotation increases. In addition, the grain orientations were randomized and no clear texture was found. These are direct confirmations that the
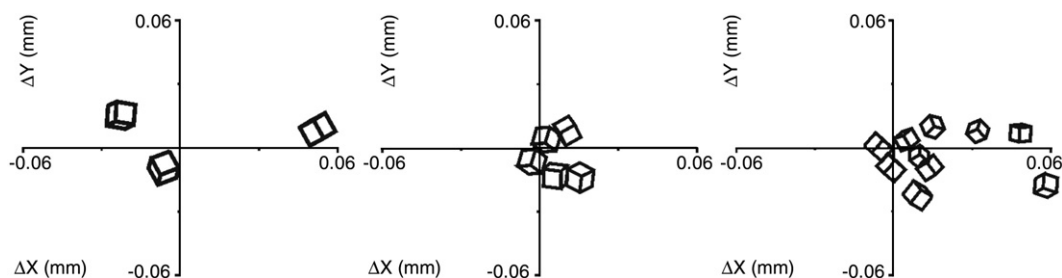

Fig. 9. Relative positions and orientations of the indexed grains at 0.2, 0.6 and 0.95 mm depth.

parameters in indexing procedure were chosen properly, since the number of successfully indexed grains reflects the real microstructure and the calculated positions of centers of diffracted grains correspond to the horizontal size of the synchrotron beam.

Typical microstrain and its corresponding microstress tensor calculated in the grain orientation system with the experimental elastic constants from Table 1 for a grain j found at 0.2 mm depth are:

$$\varepsilon(j) = \begin{pmatrix} 32.51 & 0.78 & 5.10 \\ 0.78 & -10.32 & 16.37 \\ 5.10 & -16.37 & -4.25 \end{pmatrix} *10^{-4} \quad \text{and}$$

$$\sigma(j) = \begin{pmatrix} 505 & 8.5 & 56 \\ 8.5 & 255 & -178 \\ 56 & -178 & 290 \end{pmatrix} \quad (\text{MPa}).$$

No correlation between microstresses and grain orientation could be found even after converting stresses into the specimen coordinate system. No relation was found between stresses of neighboring grains. To simplify the picture, the microstresses along the depth were represented using two rotational invariants: hydrostatic stress (p) and von Mises stress (τ). Fig. 10 shows plots of the hydrostatic stress p (Fig. 10a) and von Mises stress τ for all indexed grains (open symbols) as a function of depth. It is clear that stress in some grains attains values which exceed the macro yield stress of this alloy especially in elongated grains closer to the tracks overlapping area or interface with the substrate. The hydrostatic microstresses are spread among the neighboring grains in an almost symmetrical distribution of positive and negative values. The spread of this distribution is gradually increasing with depth when elongated grains appear in the microstructure. The mean value (close symbols) of hydrostatic stress among vicinity grains gradually decreases from tension near the top of the coating to compression at the bottom. A quite irregular picture for shear stress component is visible on Fig. 10b and it seems that overall shear component does not change significantly with depth. The clad layer can be divided in two regions. From the top until 0.6 mm, the hydrostatic stress levels spread in a constant range of about +500 to −500 MPa. From depth of 0.6 mm and further this microstress spread increases almost linearly as function of depth.

3.3. Discussion and interpretation

The characterization of macro and micro residual stress analysis by diffraction techniques present certain limitations. When the macrostrains are determined by diffraction using a constant wavelength radiation registered by a line detector, the peak shifts correspond to lattice strains of only grains with specific orientations, which do not necessarily correspond to the general stress state of the body. When 3DXRD microscopy is applied, all orientations are used for the strain/stress calculations but not necessarily all grains are detected via the indexing procedure. This may be the case of heavily deformed grains or

grains with altered composition discussed below. The situation in Co-based laser clad coating is also complicated by the dendritic character of the microstructure of Co-rich grains (see Fig. 4b). The individual γ-Co dendrites are 1–10 µm in size and are separated by a eutectic of almost the same dimensions. Because, the area of the incident synchrotron beam is 30×20 µm one may expect that the strain inside individual dendrites is measured rather than the strain over the entire grain.

When three-dimensional residual stresses are evaluated by X-ray diffraction techniques the reference parameter for strain calculations should be used with caution. For such experiments, an accurate value of stress-free lattice spacing is required that is usually found in fine powdered materials. In the case of metals and alloys, powder samples with the same properties as the irradiated volume are not always available. In this investigation the cladding alloy powder was used as reference. Since the second laser track was low in dilution, it is reasonable to assume that the overall composition of the original alloy is conserved. It became clear from the softening effects registered by micro-hardness and scratch test, Figs. 6 and 7, that local compositional variation caused by the non-homogeneous mixing of molten
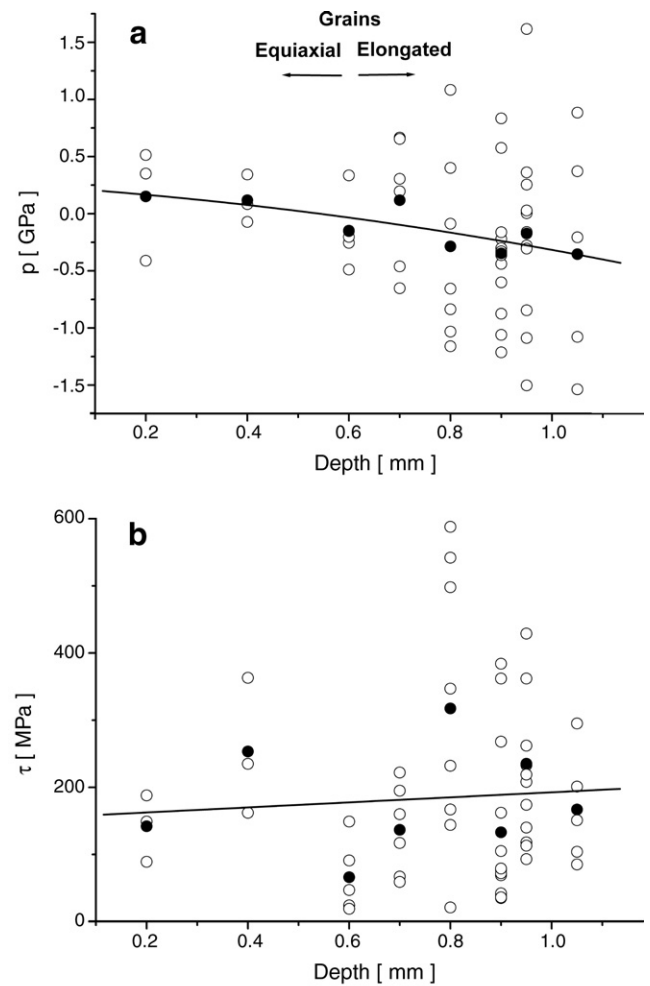

Fig. 10. a) Hydrostatic and b) von Mises intergranular microstresses of indexed γ-Co grains in function of laser coating depth. Close symbols (●) refer to the average value of the invariants at respective depth.

material resulted in Fe rich bands inside the laser tracks overlap area. As the stress-free lattice Co-based alloy powder was used as reference, incorrect residual strains may be measured when iron rich grains were indexed. A rough estimation of the dilution influence is based on a simple comparison of lattice parameters of γ-Co and γ-Fe. Lattice parameter of γ-Fe is about 1.6% larger than lattice parameter of γ-Co. If one assume I: 25% dilution of Fe in γ-Co inside these narrow dilution bands observed in Fig. 6 and II: a linear change of the lattice parameter with an amount of diluted iron, than one may expect that the lattice strain due to dilution will be on the level of 40.10^{-4}. This is a relative high value in comparison with calculated microstrains presented in Section 3.2. However, it was proved by EDS that the overall dilution was lower than 5% and that bands with higher Fe dilution are relatively narrow and perpendicular to the much larger γ-Co grains. Actually, only a few grains (around 10% of the total) at larger depths than 0.6 mm showed non-realistic strains. These grains were excluded from further analysis and are considered as highly diluted grains located in the dilution bands mentioned above. In the rest of the grains one may expect a small contribution of dilution to the experimental error of residual strain. In previous work [15], when similar experimental conditions were used to measure the strain tensor during the tensile loading of Cu polycrystal, the experimental error of strain on the level of 10^{-4} was confirmed. In a first approximation a similar level of experimental error may be expected in our experiment and in addition some systematic errors are expected due to the uncertainty in the behavior of d_o as a function of the laser track depth. It is necessary to note that a variation of d_o may originate not only from dilution of substrate Fe, but also from microstructural changes induced by thermal treatment inside a heat-affected zone during laser track overlapping. Complexity of these processes together with a lack of information what the real local d_o value is makes an estimation of the magnitude of the experimental error less reliable.

Nevertheless, it is possible to draw some conclusions on the relation between microstresses and microstructure formation by comparing Fig. 10 and corresponding microstructural characterization by OIM. It is observed that the equiaxial coarser grains localized on the upper part of the coating undergo a constant spread of stress while the finer and columnar grains from the lower part present an increasing spread of hydrostatic stress values as a function of depth. In a single phase, polycrystalline, material the intergranular microstrains are caused by inhomogeneous distribution of elastic properties localized in a stress field. As consequence, type II microstresses may present large variations due to anisotropy in individual grains oriented differently to the macro stress field. For instance, in [24] the dependence of (hkl)s for f.c.c. materials in uniaxial loading was calculated and a large difference in the strain response for diverse cubic materials was observed. In [25] a cold rolled steel was investigated and stress variation from tension to compression in neighboring grains was detected, like in the figure mentioned above.

The analysis of stress distribution is complex because of the three dimensional anisotropy of the microstructure formation. In a single clad track the preferential grain growth directions lie normal to the solidification front towards a single point. These directions are the heat flow directions, and the single point represents the center of the laser beam. Hence, on the perpendicular cross-section the grains presented random orientation, see Fig. 5. Other phenomena, such as shrinkage of the melt, phase transformations, interactions of the neighboring grains and thermomechanical deformations, will contribute for the dynamical scenario where intergranular residual stresses are generated. For the investigation of the grain-oriented-residual-stress-dependence (ODRS) a statistical number of strains as function of the grains orientations can be accessed by immersing the whole clad sample in the radiation and resolving the stresses in Euler space for the construction of Stress Orientation Distribution Function, SODF [25,26]. In this work synchrotron microbeam diffraction technique was used and therefore a statistical number of data for SODF analysis is not achieved. Instead, information about position, orientation and the strain state of individual grains is gained.

The distribution of microstresses inside Co-based laser coating measured by 3DXRD microscopy looks to be very dispersive, i.e. stresses change from one grain to another considerably and the overall trend in macrostress state observed in our previous work [16] seems to be preserved. The mean value of observed hydrostatic stress in all grains at specific laser track depth is gradually changed from tensile state in the upper part of the coating to the compressive state in its lower part close to the substrate (see Fig. 10a.). On the other hand the average value of shear stress component does not show any substantial change with depth.

4. Conclusions

The microstructural and 3DXRD microscopy observations of laser deposited Eutrolloy16012 Co-based coating together with mechanical tests leads to the following conclusions.

Laser cladding of Eutrolloy 16012 powder with an overlapping of individual laser tracks forms the thick coating on steel substrate with a sharp interface between clad layer and substrate with metallurgical bond and without any pores or macrodefects. The clad consists of fine primary γ-Co dendtrites with a eutectic interdendritic space between them. Grain size and shape strongly depend on the location in the coating. Grains close to the coating surface are coarse and equiaxial while the grains in overlapping area or closer to the coating/substrate interface are smaller and elongated in one direction. The drop in the hardness inside overlapped area is caused by microstructural changes in heat-affected zone together with the presence of iron rich bands originated from steel substrate and formed by melt convection flow during laser processing.

The residual microstrains were accessed with high spatial resolution defined by the size of the synchrotron microbeam. In this experiment, γ-Co rich grains were successfully identified and localized in the microstructure with agreement to the microstructural observations. Type II residual strains and stresses were analyzed in terms of tensor invariants, hydrostatic and von Mises shear stress, along the depth of a slightly diluted

clad track. The upper part of the coating shows a constant spread of hydrostatic stresses between -500 and 500 MPa; towards the bottom of the track the spread of these stresses increases almost linearly with depth. Behavior of overall macrostress determined as an average of these microstresses shows an already observed trend [16] when tensile stresses at the top of the coating are gradually changed to the compressive stresses near the coating/substrate interface.

Acknowledgments

References

[1] W.M. Steen, V.M. Weerasinghe, P. Monson, High Power Lasers Their Ind. Appl., SPIE 650 (1986) 226.
[2] R. Vilar, J. Laser Appl. 11 (1999) 64.
[3] M. Pilloz, J.M. Pelletier, A.B. Vannes, J. Mater. Sci. 27 (1992) 1240.
[4] R.A. Owen, R.V. Preston, P.J. Withers, H.R. Shercliff, P.J. Webster, Mater. Sci. Eng., A Struct. Mater.: Prop. Microstruct. Process. 346 (2003) 159.
[5] D. Dye, H.J. Stone, R.C. Reed, Curr. Opin. Solid State Mater. Sci. 5 (2001) 31.
[6] A. Pyzalla, Phys., B Condens. Matter 276–278 (2000) 833.
[7] G. Maeder, J.L. Lebrun, J.M. Sprauel, NDT Int. 14 (5) (1981) 235.
[8] U. Welzel, J. Ligot, P. Lamparter, A.C. Vermeulen, E.J. Mittemeijer, J. Appl. Crystallogr. 38 (2005) 1.
[9] A. Stacey, H.J. Macgillivary, G.A. Webster, P.J. Webster, K.R.A. Ziebeck, J. Strain Anal. Eng. Des. 20 (1985) 93.
[10] P.J. Withers, M. Preuss, P.J. Webster, D.J. Hughes, A.M. Korsunsky, Mat. Sci. Forum 404–407 (2002) 1.
[11] H.F. Poulsen, Three Dimensional X-ray Diffraction Microscopy, Springer-Verlag, Berlin-Heildelberg, 2004.
[12] E.M. Lauridsen, S. Schmidt, R.M. Suter, H.F. Poulsen, J. Appl. Crystallogr. 34 (2001) 744.
[13] H.F. Poulsen, L. Margulies, S. Schmidt, G. Winther, Acta Mater. 51 (2003) 3821.
[14] X. Fu, H.F. Poulsen, S. Schmidt, S.F. Nielsen, E.M. Lauridsen, D.J. Jensen, Scr. Mater. 49 (2003) 1093.
[15] L. Margulies, T. Lorentzen, H.F. Poulsen, T. Leffers, Acta Mater. 50 (2002) 1771.
[16] U. de Oliveira, V. Ocelík, J.Th.M. De Hosson, Surf. Coat. Technol. 201 (2006) 533.
[17] H.W. Press, A.A. Teukolsky, W.T. Vetterling, B.P. Flannery, Numerical Recipes in FORTRAN, The Art of Scientific Computing, second ed. University Press, Cambridge, 1992.
[18] A. Lodini, in: M.E. Fitzpatrick, A. Lodini (Eds.), Analysis of Residual Stress by Diffraction Using Neutron and Synchrotron Radiation and Evaluation, Taylor and Francis, London, 2003, p. 47.
[19] R.F.S. Hearmon, Rev. Mod. Phys. 18 (1946) 409.
[20] P. Söderlind, R. Ahuja, O. Ericsson, Phys. Rev., B 50 (1994) 5918.
[21] J.L. de Mol van Oterloo, J.Th.M. De Hosson, Acta Mater. 45 (1997) 1225.
[22] W. Kurz, D.J. Fisher, Fundamentals of Solidification, Trans Tech Publications LTD, Switzerland, 1986.
[23] H.J. Hegge, J.Th.M. De Hosson, J. Mater. Sci. 26 (1991) 711.
[24] B. Clausen, T. Lorentzen, T. Leffers, Acta Mater. 46 (1998) 3087.
[25] Y.D. Wang, R. Lin Peng, X.-L. Wang, R.L. McGreevy, Acta Mater. 50 (2002) 1717.
[26] Y.D. Wang, H. Tian, A.D. Stoica, X.-Li Wang, P.K. Liaw, J.W. Richardson, Nat. Mater. 2 (2003) 101.